to do, computationally inexpensive and provides a great deal of information. As can be noted from Eq. (9), the loss due to free carrier absorption (FCA), which affects the efficiency η, scales only with the ratio $\frac{\tau_{FC}}{Q_o}$, i.e. the ratio of free carrier lifetime to cavity photon lifetime. This again simplifies exploration of the design space.

In Fig. 6, we show simulation results for the silicon microcavity at 1550 nm in Table 2 with an example set of free carrier lifetimes and cavity loss Q values. The plot shows that, with FCA present, the optimum design's conversion efficiency, η_{max}, does not monotonically increase with input pump power, as was the case with all of the models in the previous sections (a simple explanation is provided in Appendix 13.1). This is because a stronger pump produces a larger steady-state carrier concentration generated by TPA and, as a result, the overall FCA and total cavity loss is higher at higher pump power. In fact, the free carrier loss increases faster (quadratically with pump power) than the parametric gain (linearly with pump power), leading to falling conversion efficiency with increasing pump power. Figure 6 also shows, however, that even silicon OPOs at 1550 nm, where TPA and FCA work against the nonlinear conversion process, can achieve conversion efficiencies of 0.1% with a pump power of 0.21 mW and free carrier lifetime of 60 ps, which is well within the achievable using carrier sweepout via e.g. a reverse biased p-i-n diode integrated in the optical microcavity [23]. These results and model provide some guidance for future work on efficient implementations of silicon OPOs at 1550 nm, where TPA and FCA are important.

Finally, although the optimum design is not provided in closed form for the model that includes full TPA and FCA, we can derive a closed form expression for the minimum oscillation threshold, which is now different, while it was the same in all previous sections. When FCA is present, the minimum oscillation threshold is (see Appendix 13)

$$P_{th,min} = \frac{4(1-\sigma_3)}{\left[(1-2\sigma_3)+\sqrt{(1-2\sigma_3)^2-\sigma_3\rho'_{FC}}\right]^2} P_{th,lin,min} \tag{32}$$

and depends on only the nonlinear loss sine σ_3, and normalized free-carrier-lifetime, ρ'_{FC} [see Eq. (9)]. The threshold given by this equation is consistent with the simulation results in Fig. 6. In Fig. 7(a), we plot the minimum OPO threshold versus the nonlinear loss sine σ_3 and normalized free-carrier lifetime ρ'_{FC}. We also plot the minimum OPO threshold for a silicon cavity near 1550 nm versus actual free carrier lifetime in Fig. 7(b), showing that there is a free-carrier

Fig. 7. The OPO threshold vs (a) normalized free carrier lifetime and σ_3; (b) free carrier lifetime for silicon cavity resonant near 1550 nm with linear unloaded Q of 10^6 and effective volume of $8.4\,\mu m^3$.

lifetime above which oscillation is not possible at any pump power. We expect this general result for oscillation threshold to also be a useful tool for efficient design of integrated photonic OPOs.

8. Cavity mode topology and effective figure of merit

In the introduction and coupled-mode theory model (Sections 1–3), we allowed for general mode and excitation configurations, through the topological d-vector. However, in our analysis thus far, in Sections 4–7, for simplicity we chose a single-cavity traveling-wave resonant mode system, e.g. a microring resonator excited in traveling-wave mode. That analysis is strictly valid if dispersion is such that conversion to resonances adjacent to the pump resonance dominates, i.e. if the system is effectively a three resonance system, but the primary purpose is to illustrate the major parameters that influence the efficiency, optimal choices in design, and performance scaling.

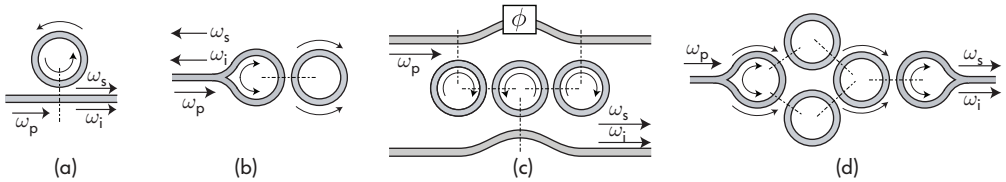

Fig. 8. Example microring cavity topology for illustration of effective figure of merit: (a) single-ring cavity with traveling-wave mode; (b)single-ring cavity with standing-wave mode; (c) triple-ring cavity with traveling-wave mode; (d)triple-ring cavity with standing-wave mode.

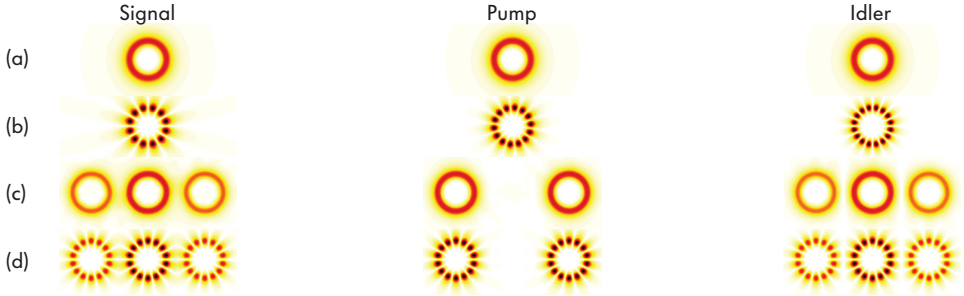

Fig. 9. Mode fields of the pump, signal and idler resonances for the configurations (a)–(d) in Fig. 8 (color–coded intensity scales are different in single and triple-cavity cases in order to show the mode features clearly).

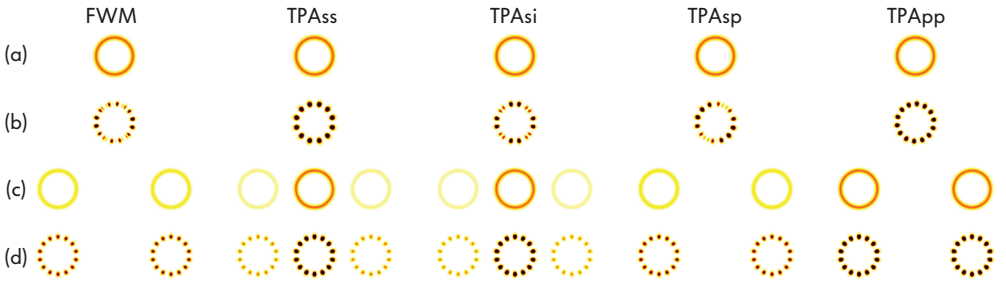

Fig. 10. Mode overlap integrand for the FWM and various TPA coefficients for configurations (a)–(d) in Fig. 8. It shows that a vector of FOM is needed to account for the ratio of FWM relative to various TPA terms. Besides, different cavity topologies have different FOM (see Table 3).

In this section, we address more general resonator configurations, such as that proposed in Fig. 1(c), and the degrees of freedom made available through engineering of coupled-cavity compound resonators and of wavelength or mode selective coupling. This is done by considering the cavity-mode topology d-vector, which we introduced in Section 3.

First, a triple-cavity resonator such as that in Fig. 1(c) is one example of a resonator that explicitly provides only 3 resonant modes near each longitudinal resonance of the constituent microring cavities. The wavelength spacing of these resonances is determined by ring-ring coupling strength, via the coupling gap [25, 22]. If the dispersion in the building-block microring cavity is sufficiently large, adjacent longitudinal resonances that are spaced 1 free spectral range (FSR) from the utilized resonance will not have proper frequency matching and will not exhibit substantial FWM as a result. Thus, the nonlinear optics can be confined to the "local" three resonances formed by ring coupling at one longitudinal order. One benefit of the triple-cavity design is that, even if the microring cavity is dispersive and has non-constant FSR, the coupling-induced frequency splitting can be designed to provide equally spaced resonances to enable FWM. As a result, the individual microring cavity can be optimized for parametric gain, without a competing requirement to produce zero dispersion, while the coupling provides the choice of output signal/idler wavelengths. By contrast, in a single-ring microcavity, the choice of wavelengths is directly coupled to the size, as is parametric gain, so minimizing the mode volume also requires one to use signal/idler wavelengths that are spaced far apart due to the large FSR, and may put a limit on how small the cavity can be made and still provide a benefit, as dispersion may begin to work against the increase in parametric gain.

Compound resonator designs can also provide substantial freedom in engineering of mode-selective coupling to the bus waveguide(s). A single-ring cavity can have wavelength-selective coupling, e.g. using a Mach-Zehnder, two-point coupler [38]. However, mode interferometry and orthogonal excitation can provide substantial control of coupling in compound resonators, such as that in Fig. 8(c). In the illustration, for example, the bottom waveguide couples only to the signal and idler resonances, because only the signal and idler resonances have non-zero intensity in the middle ring cavity [see Fig. 9(c)]. If the phase shift ϕ is chosen so that excitation of the first and last ring are out of phase for the signal/idler resonances, then they will not be excited. Since the pump resonance has antisymmetric amplitudes in the outer rings, unlike the signal and idler which have symmetric amplitudes, the pump will be efficiently excited by the same configuration, with coupling strength controlled by the choice of coupling gaps. In this way, the coupling to the pump, and to the signal and idler wavelengths, is entirely decoupled. The waveguide-resonator coupling gap in each case determines the corresponding linewidth, allowing different pump and signal/idler couplings to be implemented, as is required (as shown in earlier sections) to achieve an optimal design. Note that in this design, in the ideal scenario, the pump resonance is coupled to only the top waveguide, and the signal/idler resonances only to the bottom waveguide. Therefore, in the linear regime, the top and bottom waveguides are entirely uncoupled, and the only energy coupling from the top to the bottom waveguide can come from nonlinear interaction. One useful feature is that this design automatically filters the pump. In practice, with fabrication variations and loss, we would expect 10-20 dB rejection of the pump to be readily achievable, instead of complete decoupling, but this can still provide a useful function in parametric oscillators.

Next, we show how these geometries can be simply included in our analysis formalism, through the d-vector and an effective figure of merit. This allows a generalized approach to design, that produces a normalized optimal solution for each unique geometry subspace with a given d-vector and NFOM.

To simplify the analysis, we replace the six distinct TPA coefficients, $\beta_{\text{tpa,mn}}$, by four – after making the assumption that the frequency splitting $\Delta\omega = \omega_p - \omega_s = \omega_i - \omega_p$ is small, and

Table 3. Comparison of FWM and TPA coefficients in various cavity topologies

Cavity Type[a]	$\frac{\beta_{\text{fwm}}}{\beta_{\text{fwm}}(\text{1-ring,TW})}$[b]	d_{ss}	d_{pp}	d_{sp}	d_{si}
1-ring (TW[c])	1	1	1	1	1
3-ring (TW[c])	$\frac{1}{4}$	$\frac{3}{2}$	2	1	$\frac{3}{2}$
1-ring (SW[c])	$\frac{1}{2}$	3	3	2	2
3-ring (SW[c])	$\frac{3}{8}$	$\frac{3}{2}$	2	1	$\frac{3}{2}$

[a] Each constituent ring of the triple-ring cavity is identical to the single-ring cavity.
[b] Four wave mixing coefficients are normalized to that of a single-ring cavity with traveling-wave modes.
[c] TW: traveling-wave, SW: standing-wave.

that signal and idler mode confinement is similar, hence the effective two-photon absorption coefficients are about the same ($\beta_{\text{tpa,ii}} = \beta_{\text{tpa,ss}}$ and $\beta_{\text{tpa,ip}} = \beta_{\text{tpa,sp}}$).

As shown in Appendix 11, the four wave mixing coefficients $\beta_{\text{fwm,k}}$ ($k \in \{s, p, i\}$) and two-photon absorption coefficients $\beta_{\text{tpa,mn}}$ ($m, n \in \{s, p, i\}$), are dependent on the overlap integral of interacting cavity modes. For different cavities, these coefficients and their relative magnitudes can be very different. As an example, in Fig. 8 we show resonators consisting of a single ring cavity or triple coupled ring cavities, each with either traveling-wave mode or standing-wave mode excitation. The supermodes are shown in Fig. 9. In Fig. 10, we plot the parametric gain due to FWM and loss due to TPA in these microcavities. It turns out that, for example, the ratio of signal-idler TPA to parametric gain (i.e. $\sigma_3 d_{\text{si}}$) is larger in a triple-ring resonator than in a single-ring resonator, with a traveling-wave mode excitation. This means that the effective figure of merit of the triple-ring resonator is smaller than that of the single-ring cavity. A complete summary of various FWM coefficients and d-vectors is shown in Table 3.

Table 4 shows the results of Table 2 evaluated for a 3-coupled cavity "photonic molecule" OPO with traveling-wave excitation, based on the same ring cavity design in each case.

The important conclusion from this study is that the cavity *envelope* matters, i.e. the distribution of the field across parts of the compound resonator, as well as standing vs. traveling wave excitation. Specifically, standing-wave excitation is very "efficient" for self-TPA loss terms, such as absorption of two signal photons or two pump photons. On the other hand, because of differences in longitudinal mode order, the parametric gain is a bit suppressed. Thus, standing wave excitation in general loses to traveling-wave excitation in the presence of TPA. Likewise, the single-ring configuration is more efficient than triple ring with traveling-wave excitation. However, with standing-wave excitation, the single-ring resonator has a larger FWM coefficient but at the same time larger TPA loss (d coefficients). However, it should be kept in mind that this comparison is for microring cavities being equal. The triple ring design may be able to use much smaller ring cavities than a single ring design, however, as it is not limited by dispersion. Therefore, either may be more efficient, depending on specific implementation, target wavelengths, etc.

More generally, our conclusions are that higher-order resonator designs can provide both unique functionality, and access to degrees of freedom needed to produce an optimum design. The model presented provides a normalized solution vs. normalized pump power (that includes linear losses), nonlinear FOM σ_3 and a normalized FCA, for each resonator "topology" with a unique d-vector. This should provide a basis for exploring efficient device designs and novel applications.

Table 4. Predicted performance of optical parametric oscillators based on 3-ring photonic molecule with traveling-wave mode

Material	$\lambda(\mu\text{m})$	$V_{\text{eff}}(\mu\text{m}^3)^a$	$\beta_{\text{fwm}}(10^6\text{J}^{-1})$	$P_{\text{th}}(\text{mW})$
c-Si	1.55	8.3	7.2	0.29
c-Si	2.3	40	0.63	0.65
a-Si:H	1.55	8.3	46	0.015
Si_3N_4	1.55	337	0.05	11

[a] Each constituent ring of the triple-ring cavity is identical to the single-ring cavity in Table 2.

9. Future work

The purpose of this paper was to lay the theoretical foundation for designing efficient parametric oscillators, and for considering the degrees of freedom made available in design by complex photonic structures such as coupled-cavity resonators. A number of details will play an important role in determining the practical utility of these designs. For example, we have here assumed that ring-ring coupling is lossless. In practice, couplers exhibit radiation loss [39, 40] and will limit the performance of coupled-cavity designs for FWM. Design details such as this will be specific to particular implementations, and are left for future study.

Furthermore, we considered the optimal case here with perfect frequency matching. In an experimental situation, a frequency mismatch must be admitted, and this requires only a simple modification of the presented model.

More generally, the degrees of freedom available in coupled resonant structures on chip suggest that complex synthesis and designs will enable either optimal designs or ones with unique capability for other applications, such as parametric amplifiers and entangled photon sources, including design of joint spectral and temporal distribution of the bi-photons, their coincidence properties, etc.

The distributed states formed in coupled-cavity resonators suggest an analogy to distributed electronic states in molecules, so we sometimes refer to these structures as “photonic molecules”. What is unique, in comparison to atomic molecules, is that here we can engineer the resonant frequencies (energies) of the distributed states, their overlap integrals (for purposes of nonlinear optics) by choice of coupling geometries, their effective “absorption and emission cross-sections” to waveguides via choice of coupling. Beyond degrees of freedom available in natural molecules, we can further design anisotropic absorption and emission, i.e. couple different wavelength resonances to entirely separate radiation channels of waveguides.

More generally, there exist coupled cavity geometries that provide unique state manipulation that is either non-existent or unusual in natural atomic molecules, such as radiative coupling which leads to energy-level attraction, in contrast to the usual energy level repulsion [17, 41]. Such devices can even have splitting in the radiative lifetime instead of energy level, i.e. resonant frequency. Such designs likewise may have applications in single photon sources and unique types of laser cavities [41].

10. Conclusion

Generally, the results in this paper show that efficient micro-OPOs can be designed in the presence of only linear losses, and even with limited nonlinear losses, as well as free carrier absorption. Notably, while devices without TPA call for equal optimum external coupling to all three resonances when the pump is far above threshold, we show that both in the case closer to the threshold, and in the case with substantial nonlinear losses, it is necessary to design substantially different signal/idler, and pump resonance external coupling for optimum performance.

In the case where nonlinear losses are present, we have shown that a large set of practical cases can be solved by considering only pump-induced TPA. In this case, we provide an analytical solution to the design. With full (pump and signal/idler induced) TPA, and with FCA loss included, more complex models do not admit simple closed-form solutions. However, we provide a normalized set of design equations, based on which we can numerically solve for the optimum design, and provide a single set of normalized design plots relevant for design using all nonlinear materials, linear cavity losses, and pump powers.

These results have also motivated our proposal of both spatial mode and Q engineered multimode resonators, based on multiple coupled cavities, for nonlinear FWM applications [22]. The requirements of an optimum OPO design presented here, primarily the different external coupling for pump and signal/idler resonances suggested by the results, do not fit well with a simple linear cavity such as a Fabry-Perot resonator, or a microring cavity, with broadband coupling to an external excitation port (via a mirror, or directional coupler, respectively). Yet, such designs have been common in tabletop OPOs [26] as well as on-chip OPOs in silicon and silicon nitride [10, 7]. We believe this analysis suggests further work on more advanced geometries (such as Fig. 1(c)) may enable more efficient designs, and may enable one to reach the performance bounds found in this paper.

This work also suggests that complex photonic circuits may provide useful solutions not only for OPOs but also for other devices including parametric amplifiers and entangled photon sources. A large amount of research was done in the early to mid 1900's in electrical circuit linear filter synthesis using resistors, capacitors and inductors, leading to a body of sophisticated linear filter design techniques. Development of synthesis of nonlinear circuits based on resonators as building block components may yield a similarly rich array of solutions to nonlinear optics design on chip.

11. Appendix A: Mode overlap integrals

For plane wave propagating in bulk medium, the FWM coefficient, β_{fwm}, is directly related to the third-order susceptibility of the nonlinear material, $\overline{\overline{\chi}}^{(3)}$. In a microphotonic structure, the optical fields are tightly confined and the FWM coefficient also depends on an overlap integral of the interacting mode fields, given by [24, 31]

$$\beta_{\text{fwm,s}} = \frac{\frac{3}{16}\varepsilon_0 \int d^3\mathbf{x} \left(\mathbf{E}_s^* \cdot \overline{\overline{\chi}}^{(\mathbf{3})} : \mathbf{E}_p^2 \mathbf{E}_i^*\right)}{\sqrt{\int d^3\mathbf{x} \left(\frac{1}{2}\varepsilon |\mathbf{E}_s|^2\right) \int d^3\mathbf{x} \left(\frac{1}{2}\varepsilon |\mathbf{E}_i|^2\right)} \int d^3\mathbf{x} \left(\frac{1}{2}\varepsilon |\mathbf{E}_p|^2\right)} \equiv \frac{3\chi^{(3)}_{1111}}{4n_{\text{nl}}^4 \varepsilon_0 V_{\text{eff}}} \tag{33}$$

where n_{nl} is the refractive index of nonlinear material, ε_0 is vacuum permittivity, V_{eff} is effective volume given by

$$V_{\text{eff}} \equiv \frac{\chi^{(3)}_{1111} \sqrt{\int d^3\mathbf{x} \left(\varepsilon |\mathbf{E}_s|^2\right) \int d^3\mathbf{x} \left(\varepsilon |\mathbf{E}_i|^2\right)} \int d^3\mathbf{x} \left(\varepsilon |\mathbf{E}_p|^2\right)}{\varepsilon_0^2 n_{nl}^4 \int d^3\mathbf{x} \left(\mathbf{E}_s^* \cdot \overline{\overline{\chi}}^{(\mathbf{3})} : \mathbf{E}_p^2 \mathbf{E}_i^*\right)}. \tag{34}$$

The effective volume, V_{eff}, is the equivalent bulk volume of nonlinear medium, in which uniform fields with the same energy would have equal nonlinearity (β_{fwm}). With the full permutation symmetry of $\overline{\overline{\chi}}^{(3)}$, we have $\beta_{\text{fwm,s}} = \beta_{\text{fwm,i}} = \beta^*_{\text{fwm,p}}$ (the Manley-Rowe relations).

The nonlinear loss coefficients due to two-photon absorption, $\beta_{\text{tpa,mn}}$ (due to absorption of a photon each from modes m and n, $m,n \in \{s,p,i\}$), are described by similar overlap integral. For example,

$$\beta_{\text{tpa,sp}} = \frac{\frac{3}{16}\varepsilon_0 \int d^3\mathbf{x} \left(\mathbf{E}_s^* \cdot \Im[\overline{\overline{\chi}}^{(\mathbf{3})}] : \mathbf{E}_s \mathbf{E}_p \mathbf{E}_p^*\right)}{\int d^3\mathbf{x} \left(\frac{1}{2}\varepsilon |\mathbf{E}_s|^2\right) \int d^3\mathbf{x} \left(\frac{1}{2}\varepsilon |\mathbf{E}_p|^2\right)}. \tag{35}$$

12. Appendix B: Free carrier absorption rate

Here we derive the loss rate of cavity mode amplitude envelop (A_k in the CMT model, for $k \in s,p,i$) due to free carrier absorption induced by two-photon absorption [see Eq. (4)]. On the one hand, free carriers are created through TPA with equal densities. In general, the dynamics of free carrier density, N_ν, is governed by the continuity equation [42]

$$\frac{\partial N_\nu}{\partial t} = G - \frac{N_\nu}{\tau_\nu} + D_\nu \nabla^2 N_\nu - s_\nu \mu_\nu \nabla \cdot (N_\nu \mathbf{E}_{\rm dc}) \equiv G - \frac{N_\nu}{\tau_{\nu,\rm eff}} \tag{36}$$

where $\nu = e$ for electrons, $\nu = h$ for holes, $s_h = 1$, $s_e = -1$, D_ν is the diffusion coefficient, μ_ν is the mobility, $\mathbf{E}_{\rm dc}$ is applied dc electric field, τ_ν is the carrier lifetime, and $\tau_{\nu,\rm eff}$ is the effective carrier lifetime that includes all the effects of recombination, diffusion and drift. G is the free carrier generation rate per volume due to TPA, where one pair of electron and hole is generated for every two photons absorbed

$$G = \frac{1}{2\hbar\omega}\frac{\Delta E}{\Delta t \cdot \Delta V} = \frac{1}{4\hbar\omega}\Re[\mathbf{E}^*_{\rm tot}\cdot\mathbf{J}] = \frac{1}{4\hbar\omega}\Re[j\omega\varepsilon_0\mathbf{E}^*_{\rm tot}\cdot\overline{\overline{\chi}}^{(3)} : \mathbf{E}^3_{\rm tot}] \tag{37}$$

where $\mathbf{E}_{\rm tot}$ is total electric field ($\mathbf{E}_{\rm tot} = \mathbf{E}_{\rm s} + \mathbf{E}_{\rm p} + \mathbf{E}_{\rm i}$). Thus the steady-state free carrier density is given by

$$N_\nu = G\tau_{\nu,\rm eff}. \tag{38}$$

On the other hand, these free carriers contribute to optical loss. The free carrier absorption coefficient of optical power (absorption rate per distance) is

$$\alpha_\nu = \sigma_\nu N_\nu \tag{39}$$

where σ_ν is free carrier absorption cross section area. Note that both $\tau_{\nu,\rm eff}$ and G are position-dependent, and therefore the free carrier absorption coefficient α_ν is non-uniform across the waveguide cross section. Besides, the optical field intensity is also non-uniform. As a result, the interplay between free carriers and optical field needs to be studied carefully. If the field decay rate due to free carrier loss is much smaller than the cavity resonance frequency, we can include the FCA loss into the perturbation theory of CMT model, with the free carrier loss rate of mode k (for $k \in s,p,i$) due to free carrier ν as

$$\begin{aligned} r^\nu_{\rm k,FC} &= -\frac{j\omega}{4}\frac{\int d^3\mathbf{x}\left(\mathbf{E}^*_{\rm k}\cdot\delta\mathbf{P}^{(\rm FCA,\nu)}_{\rm k}\right)}{\int d^3\mathbf{x}\left(\frac{1}{2}\varepsilon|\mathbf{E}_{\rm k}|^2\right)} = \frac{\omega}{4}\frac{\int d^3\mathbf{x}\left(\varepsilon_0 n_{\rm nl}\frac{\alpha_\nu}{k_0}|\mathbf{E}_{\rm k}|^2\right)}{\int d^3\mathbf{x}\left(\frac{1}{2}\varepsilon|\mathbf{E}_{\rm k}|^2\right)} \\ &= \frac{\varepsilon_0 n_{\rm nl}\omega\sigma_\nu}{4k_0}\frac{\int d^3\mathbf{x}\left(G\tau_{\nu,\rm eff}|\mathbf{E}_{\rm k}|^2\right)}{\int d^3\mathbf{x}\left(\frac{1}{2}\varepsilon|\mathbf{E}_{\rm k}|^2\right)} = \frac{c\varepsilon_0^2 n_{\rm nl}\sigma_\nu}{16\hbar}\frac{\int d^3\mathbf{x}\left(\tau_{\nu,\rm eff}(\mathbf{E}^*_{\rm tot}\cdot\Im[\overline{\overline{\chi}}^{(3)}] : \mathbf{E}^3_{\rm tot})|\mathbf{E}_{\rm k}|^2\right)}{\int d^3\mathbf{x}\left(\frac{1}{2}\varepsilon|\mathbf{E}_{\rm k}|^2\right)}. \end{aligned} \tag{40}$$

This expression for free carrier absorption rate is true, but very complex to solve. We make some assumptions to simplify the expression above. First, we assume the effective free carrier lifetime, $\tau_{\nu,\rm eff}$, is the same for electrons and holes. Second, we assume the steady-state free carrier density generated by TPA is uniform (invariant with respect to position) in the cavity. This assumption is valid when the carrier density equilibrates due to a diffusion that is much faster than recombination [43], or a fast drift due to an applied field for carrier sweep-out. With these assumptions, we use the effective volume of nonlinear interaction, $V_{\rm eff}$ (defined in Appendix 11), to average out the free carrier density, N_ν. From Eqs. (1a)-(1c), using

$\frac{\partial N_v}{dt} = -\frac{N_v}{\tau_{\text{eff}}} + \frac{1}{2\hbar\omega V_{\text{eff}}}\frac{d|A_k|^2}{dt} = 0$, we have

$$N_v = \frac{\tau_{\text{eff}}}{\hbar V_{\text{eff}}}\left(\beta_{\text{tpa,ss}}|A_s|^4 + \beta_{\text{tpa,pp}}|A_p|^4 + \beta_{\text{tpa,ii}}|A_i|^4 + 4\beta_{\text{tpa,sp}}|A_s|^2|A_p|^2 + 4\beta_{\text{tpa,ip}}|A_i|^2|A_p|^2 + 4\beta_{\text{tpa,si}}|A_s|^2|A_i|^2\right). \tag{41}$$

The optical field decay rate due to FCA is given by

$$r_{\text{FC}} = \frac{\alpha_{\text{FC}} v_g}{2} = \frac{\sigma_{\text{a}} N_v v_g}{2} = \frac{\tau_{\text{eff}}\sigma_{\text{a}} v_g}{2\hbar V_{\text{eff}}}\left(\beta_{\text{tpa,ss}}|A_s|^4 + \beta_{\text{tpa,pp}}|A_p|^4 + \beta_{\text{tpa,ii}}|A_i|^4 + 4\beta_{\text{tpa,sp}}|A_s|^2|A_p|^2 + 4\beta_{\text{tpa,ip}}|A_i|^2|A_p|^2 + 4\beta_{\text{tpa,si}}|A_s|^2|A_i|^2\right) \tag{42}$$

where σ_{a} is the free carrier absorption cross section area, including contributions from both free electrons and holes, v_g is group velocity of optical modes. σ_a and v_g both only have a meaning in the context of resonators formed from a waveguide, such as microring or waveguide Fabry-Perot resonators. The expression is still valid for 3D standing wave cavities such as photonic crystal microcavities, where only the product $\sigma_a v_g$ as a whole has a unique physical meaning.

13. Appendix C: Minimum threshold pump power

In this section we derive the minimum threshold pump power of optical parametric oscillation in a single ring cavity with traveling-wave mode. From Eqs. (12)–(13):

$$T_{\text{p},+} = j\left(\sqrt{2\rho_{\text{p,ext}}}\right)^{-1}\left(\rho_{\text{p,tot}} + 8\rho_{\text{i,tot}}^{-1}|B_s|^2|B_p|^2\right)B_p. \tag{43}$$

When the input pump power is just above threshold, the OPO starts lasing, $|B_s|^2 \approx 0$, and thus

$$|T_{p,+}|^2 = \frac{\rho_{\text{p,tot}}^2}{2\rho_{\text{p,ext}}}|B_p|^2 \tag{44}$$

The threshold pump power is the smallest pump power that can make the OPO oscillate. To minimize threshold, we can choose external coupling for pump, signal and idler to minimize the expression for pump power above [see Eq. (44)]. The pump power is minimized at

$$\rho_{\text{p,ext}} = 1 + 2\sigma_3|B_p|^2 + \sigma_3\rho'_{\text{FC}}|B_p|^4 \tag{45}$$

and

$$P_{\text{th}} = \left(2(1 + 2\sigma_3|B_p|^2 + \sigma_3\rho'_{\text{FC}}|B_p|^4)|B_p|^2\right)_{\text{min}} \tag{46}$$

So we need to minimize $|B_p|^2$. From Eqs. (11) and (12)

$$2|B_p|^2 = \rho_{\text{s,tot}} = 1 + \rho_{\text{s,ext}} + 4\sigma_3|B_p|^2 + \sigma_3\rho'_{\text{FC}}|B_p|^4 \tag{47}$$

By solving this quadratic equation, we have the smaller root:

$$|B_p|^2 = \frac{(1-2\sigma_3) - \sqrt{(1-2\sigma_3)^2 - \sigma_3\rho'_{\text{FC}}(1+\rho_{\text{s,ext}})}}{\sigma_3\rho'_{\text{FC}}} \tag{48}$$

To minimize $|B_p|^2$, we have $\rho_{\text{s,ext}} = 0$. And there is an upper limit of normalized FCA loss for OPO to oscillate:

$$\rho'_{\text{FC}} \leq \frac{(1-2\sigma_3)^2}{\sigma_3} \tag{49}$$

By putting Eq. (48) into Eq. (46) we have the threshold pump

$$P_{\text{th}} = \frac{4(1-\sigma_3)}{\left((1-2\sigma_3)+\sqrt{(1-2\sigma_3)^2-\sigma_3\rho'_{\text{FC}}}\right)^2} \tag{50}$$

It is easy to prove that in the no FCA loss limit ($\rho'_{\text{FC}} \to 0$), the threshold pump power simplifies to Eq. (17). This choice of external coupling makes sense, as it corresponds to maximum parametric gain (the largest in-cavity pump light energy for given input pump power) and the smallest loss rate for the signal and idler light.

For the case of equal pump and signal/idler coupling ($\rho_{\text{p,ext}} = \rho_{\text{s,ext}} = \rho_{\text{ext}}$), Eqs. (44) and (47) can be combined to give:

$$|T_{p,+}|^2 = \frac{\rho^3_{\text{p,tot}}}{4(1-\sigma_3)\rho_{\text{ext}}} \tag{51}$$

where $\rho_{\text{ext}} = \rho_{\text{p,tot}} - 1 - 2\sigma_3|B_p|^2 - \rho'_{\text{FC}}|B_p|^4$, $|B_p|^2 = \frac{\rho_{\text{s,tot}}}{2} = \frac{\rho_{\text{p,tot}}}{2-2\sigma_3}$ and then the threshold pump power can be represented by a function of ρ_{ext}. This expression is complex, but can be simplified when FCA is ignorable:

$$P'_{\text{th}} = \frac{(1-\sigma_3)^2}{4(1-2\sigma_3)^3}\frac{(1+\rho_{\text{ext}})^3}{\rho_{\text{ext}}}|_{\text{min}} = \frac{27(1-\sigma_3)^2}{16(1-2\sigma_3)^3} \tag{52}$$

with $\rho_{\text{ext}} = 1/2$ at threshold.

13.1. Understanding oscillation threshold

Here we provide a physical interpretation of the oscillation threshold when both linear and nonlinear loss are present. Figure 11 shows the various terms of small-signal gain and loss for the signal resonance in an optical parametric oscillator based on degenerate four wave mixing. The linear loss rate, including material absorption, scattering loss, radiation loss and external coupling etc., is independent of the in-cavity pump energy, which roughly scales with input pump power. The parametric gain from four wave mixing, and loss due to two-photon absorption, are

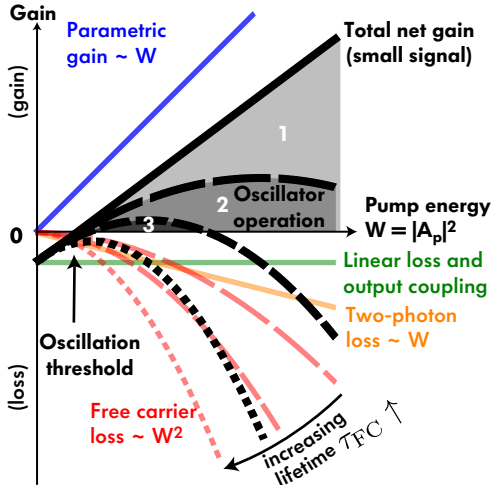

Fig. 11. Small signal gain and loss in an optical parametric oscillator based on degenerate four wave mixing.

both proportional to pump energy. However, their scaling factors vary by a factor of $2\sigma_3$, thus it is only possible to achieve oscillation for a nonlinear material with $\sigma_3 < 0.5$.

The loss due to free carrier absorption scales with the square of the pump energy, shown as parabolic curve in Fig. 11. When the loss due to free carrier absorption is ignorable, the total net gain is greater than 0 in region 1. As the effective free carrier lifetime increases, the parabolic curve becomes steeper, and the region of positive net gain shrinks to region 2 and region 3. When the free carrier lifetime is above a certain limit, the total net gain is always negative, no matter how large the pump light energy is. This is consistent with the plot of oscillation threshold in Fig. 7.

14. Appendix D: Upper bound of FWM conversion efficiency

In this section we derive an upper bound of FWM conversion efficiency limited by TPA. From Eqs. (12)–(13):

$$T_{\mathrm{p},+} = j\left(\sqrt{2\rho_{\mathrm{p,ext}}}\right)^{-1}\left(\rho_{\mathrm{p,tot}} + 8\rho_{\mathrm{i,tot}}^{-1}|B_s|^2|B_p|^2\right)B_p = A + B|B_s|^2 \tag{53}$$

Where $A \equiv j\left(\sqrt{2\rho_{\mathrm{p,ext}}}\right)^{-1}\rho_{\mathrm{p,tot}}B_p$, $B \equiv j\left(\sqrt{2\rho_{\mathrm{p,ext}}}\right)^{-1}8\rho_{\mathrm{i,tot}}^{-1}|B_p|^2B_p$. For the case of pump-only TPA and no FCA, the in-cavity pump light energy has a simple form [see Eq. (16)], and thus A and B are independent on the input pump power. The conversion efficiency is

$$\eta = \frac{2\rho_{\mathrm{s,ext}}|B_s|^2}{|T_{\mathrm{p},+}|^2} = \left(\frac{2\rho_{\mathrm{s,ext}}}{B}\right)\frac{T_{\mathrm{p},+} - A}{|T_{\mathrm{p},+}|2} \tag{54}$$

Since the phases of A, B, $T_{p,+}$ are the same, thus

$$\eta = \left(\frac{2\rho_{\mathrm{s,ext}}}{|B|}\right)\frac{|T_{\mathrm{p},+}| - |A|}{|T_{\mathrm{p},+}|^2} \tag{55}$$

It's easy to see that η is a function only of the input pump power ($|T_{\mathrm{p},+}|^2$), external coupling ($\rho_{\mathrm{k,ext}}$) and the nonlinear loss sine σ_3. Now we calculate the maximum conversion efficiency at fixed external coupling from $\frac{\partial\eta}{\partial|T_{\mathrm{p},+}|} = 0$. Then,

$$|T_{\mathrm{p},+}|^2 = 4A^2 = \frac{2\rho_{\mathrm{p,tot}}^2}{\rho_{\mathrm{p,ext}}}|B_p|^2$$

and substituting back into (55), the maximum efficiency is

$$\eta_{\max} = \frac{\rho_{\mathrm{s,ext}}}{2AB} = \frac{(1-2\sigma_3)^2}{2}\frac{\rho_{\mathrm{s,ext}}\rho_{\mathrm{p,ext}}\rho_{\mathrm{i,tot}}}{\rho_{\mathrm{p,tot}}(1+\rho_{\mathrm{s,ext}})^2} = \left(\frac{1}{2}-\sigma_3\right)\frac{\rho_{\mathrm{p,ext}}}{\rho_{\mathrm{p,tot}}}\frac{\rho_{\mathrm{s,ext}}(1+\rho_{\mathrm{i,ext}})}{(1+\rho_{\mathrm{s,ext}})^2} < \frac{1}{2}-\sigma_3. \tag{56}$$

This puts an upper bound on the achievable conversion efficiency (to each of the signal and idler), as a function of the nonlinear loss sine σ_3.

15. Appendix E: Analogy to laser oscillation

By combining Eq. (6a) and Eq. (12) we have the lasing equation for signal light

$$\frac{dB_s}{d\tau} = -\rho_{\mathrm{s,tot}}B_s + 4\rho_{\mathrm{i,tot}}^{-1}|B_p|^4B_s \equiv -\rho_{\mathrm{loss}}B_s + \rho_{\mathrm{gain}}B_s \tag{57}$$

Both the loss and gain for the signal light depend on the in-cavity pump light energy. When the loss and gain term are equal, we arrive at the expression for $|B_p|^2$ in oscillation [see Eq. (16)]. At the same time, the parametric gain also depends on in-cavity signal light energy, which results in gain clamping.

$$\frac{dB_p}{d\tau} = -\rho_{\mathrm{p,tot}} B_p - 8\rho_{\mathrm{i,tot}}^{-1} |B_p|^2 |B_s|^2 B_p - j\sqrt{2\rho_{\mathrm{p,ext}}} T_{p,+} \tag{58}$$

Acknowledgments

We thank Prof. Kelvin Wagner at University of Colorado Boulder for helpful discussions, and Cale Gentry for input on the manuscript. This work was supported in part by start-up funds from the College of Engineering and Applied Science, University of Colorado Boulder, and by the David & Lucile Packard Foundation through a Packard Fellowship in Science & Engineering. Publication of this article was partially funded by the University of Colorado Boulder Libraries Open Access Fund.